Crystalline Order in Strongly Coupled Ion Plasmas*

T. B. Mitchell, J. J. Bollinger, X.-P. Huang,† W. M. Itano, J. N. Tan,‡ B. M. Jelenković,§ and D. J. Wineland

Time and Frequency Division, National Institute of Standards and Technology, Boulder, CO 80303

Abstract. Laser-cooled trapped ions can be strongly coupled and form crystalline states. This manuscript reviews experimental studies which measure the spatial correlations of Be^+ ion crystals formed in Penning traps. Both Bragg scattering of the cooling-laser light and spatial imaging of the laser-induced ion fluorescence are used to measure these correlations. In spherical plasmas with more than 2×10^5 ions, body-centered-cubic (bcc) crystals, the predicted bulk structure, are the only type of crystals observed. The orientation of the ion crystals can be phase-locked to a rotating electric-field perturbation. With this "rotating wall" technique and stroboscopic detection, images of individual ions in a Penning trap are obtained. The rotating wall technique also provides a precise control of the time-dilation shift due to the plasma rotation, which is important for Penning trap frequency standards.

INTRODUCTION

This manuscript summarizes recent progress on the study of strongly coupled ion plasmas in Penning traps. It is similar to the review in the conference proceedings of Ref. [1] and contains more background material on Bragg-scattering results than Ref. [2], which focuses on results obtained from real images of the ion crystals.

Trapped ions are a good example of a one-component plasma (OCP). An OCP consists of a single charged species immersed in a neutralizing background [3]. In an ion trap, the trapping fields provide the neutralizing background [4]. Examples of OCPs include such diverse systems as the outer crust of neutron stars [5] and electrons on the surface of liquid helium [6]. The thermodynamic properties of the classical OCP of infinite spatial extent are determined by its Coulomb coupling constant [3]

---

*) Work of the U.S. Government. Not subject to U.S. copyright

†) Present address: Colorado MEDtech - RELA, Inc., 6175 Longbow Dr., Boulder, CO 80301

‡) Present address: Physics Dept., Harvard Univ., Cambridge, MA 02138

§) On leave from the Institute of Physics, University of Belgrade, Belgrade, Yugoslavia

CP498, *Non-Neutral Plasma Physics III,* edited by John J. Bollinger, et al.
1999 American Institute of Physics 1-56396-913-0

$$\Gamma \equiv \frac{1}{4\pi\epsilon_o}\frac{e^2}{a_{WS}k_BT}, \tag{1}$$

which is a measure of the ratio of the Coulomb potential energy of nearest neighbor ions to the kinetic energy per ion. Here, ϵ_o is the permittivity of the vacuum, e is the charge of an ion, k_B is Boltzmann's constant, T is the temperature, and a_{WS} is the Wigner-Seitz radius, defined by $4\pi(a_{WS})^3/3 = 1/n_o$, where n_o is the ion density. For low temperature ions in a trap, n_o equals the equivalent neutralizing background density provided by the trapping fields. Plasmas with $\Gamma > 1$ are called strongly coupled. The onset of fluid-like behavior is predicted at $\Gamma \approx 2$ [3], and a phase transition to a body-centered-cubic (bcc) lattice is predicted at $\Gamma \approx 170$ [3,7]. From a theoretical perspective, the strongly coupled OCP has been used as a paradigm for condensed matter for decades. However, only recently has it been realized in the laboratory [8].

Experimentally, freezing of small numbers ($N < 50$) of laser-cooled atomic ions into Coulomb clusters was first observed in Paul traps [9–11]. With larger numbers of trapped ions, concentric shell structures were observed directly in Penning [12] and linear Paul [13,14] traps. The linear Paul traps provided strong confinement in the two dimensions perpendicular to the trap axis and very weak confinement along the trap axis. This resulted in cylindrically shaped plasmas whose axial lengths are large compared to their cylindrical diameters. Cylindrical-shell crystals which are periodic with distance along the trap axis were observed. The diameter of these crystals was limited to $\sim$10 a_{WS} in Ref. [13] and $\sim$30 a_{WS} in Ref. [14], presumably due to rf heating [15] which is produced by the time-dependent trapping fields and increases with the plasma diameter. These plasma diameters appear to be too small to observe the 3-D periodic crystals predicted for the infinite, strongly coupled OCP. Strong coupling and crystallization have also been observed with particles interacting through a screened Coulomb potential. Examples include dusty plasma crystals [16] and colloidal suspensions [17,18].

Because Penning traps use static fields to confine charged particles, there is no rf heating. This has enabled ion plasmas which are large in all three dimensions to be laser-cooled. For example, we have laser-cooled $\sim 10^6$ Be^+ ions in an approximately spherical plasma with diameter $\sim 200a_{WS}$. With these large ion plasmas we have used Bragg scattering of the cooling laser light to detect the formation of bcc crystals [19,20], the predicted state for a bulk OCP with $\Gamma > 170$. In addition, we have studied the spatial correlations in planar, lens-shaped plasmas with axial thickness $\lesssim 10a_{WS}$. These plasmas consist of extended, two dimensionally periodic lattice planes. The importance of the plasma boundary in this case results in different crystalline structures depending on the details of the plasma shape.

A potential drawback of the Penning trap versus the rf trap is that the ions rotate about the trap magnetic field, and this has previously prevented the imaging of the ion crystals as done in Paul traps. This is because the rotation, created by the $\mathbf{E}\times\mathbf{B}$ drift due to the radial electric and the trap magnetic fields is, in general, not stable. For example, fluctuations in the plasma density or shape produce fluctuations in

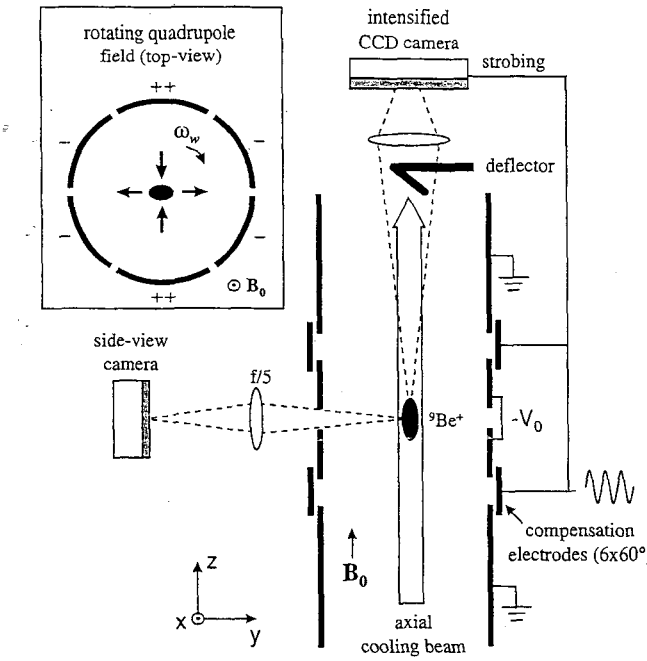

FIGURE 1. Schematic view of the cylindrical trap with real space imaging optics for the side-view camera and Bragg diffraction detection system for the axial cooling beam. The size of the plasma is exaggerated. Cross section of the rotating quadrupole field (in the x-y plane) is shown in the insert. From Ref. [21].

the ion space-charge fields which change the plasma rotation. However, we are able to phase-lock the rotation of the laser-cooled ion crystals to a rotating electric-field perturbation [21,22]. The success of this "rotating wall" technique enables us to strobe the cameras recording the ion fluorescence synchronously with the plasma rotation and obtain images of individual ions in the plasma crystals [23].

Figure 1 is a schematic of the cylindrical Penning trap we use to confine $^9Be^+$ ions. The trap consists of a 127 mm long vertical stack of cylindrical electrodes with an inner diameter of 40.6 mm, enclosed in a room temperature, 10^{-8} Pa vacuum chamber. The uniform magnetic field $\mathbf{B_o} = 4.46$ T is aligned parallel to the trap axis within 0.01° and produces a $^9Be^+$ cyclotron frequency $\Omega = 2\pi \times 7.61$ MHz. A quadratic, axially symmetric potential $(m\omega_z^2/2e)[z^2 - r^2/2]$ is generated near the trap center by biasing the central electrodes to a negative voltage $-V_o$. At $V_o = 1$ kV, the single-particle axial frequency $\omega_z = 2\pi \times 799$ kHz and the magnetron $\mathbf{E} \times \mathbf{B}$ drift frequency $\omega_m = 2\pi \times 42.2$ kHz. The trapped Be^+ ions are Doppler laser-cooled by two 313 nm laser beams. The principal cooling beam (waist diameter ~ 0.5 mm, power ~ 50 μW) is directed parallel to $\mathbf{B_o}$. A second,

typically weaker cooling beam with a much smaller waist (~ 0.08 mm) is directed perpendicularly to $\mathbf{B}_o$ (not shown in Fig. 1). This beam can also be used to vary the plasma rotation frequency by applying a torque with radiation pressure. With this configuration, ion temperatures close to the 0.5 mK Doppler laser-cooling limit are presumably achieved. However, experimentally we have placed only a rough 10 mK upper bound on the ion temperature [24]. For a typical value of $n_o = 4 \times 10^8$ cm^{-3}, this implies $\Gamma > 200$.

Two types of imaging detectors were used. One is a charge-coupled-device (CCD) camera coupled to an electronically gateable image intensifier. The other is an imaging photomultiplier tube based on a microchannel-plate electron multiplier and a multielectrode resistive anode for position sensing. For each detected photon, the position coordinates are derived from the current pulses collected by the different electrodes attached to the resistive anode. This camera therefore provides the position and time of each detected photon. However, in order to avoid saturation, we placed up to 20 dB of attenuation in front of this camera to lower the detected photon counting rate to less than ~ 300 kHz.

In thermal equilibrium, the trapped ion plasma rotates without shear at a frequency ω_r, where $\omega_m < \omega_r < \Omega - \omega_m$ [25,26]. For the low temperature work described here, the ion density is constant and given by $n_o = 2\epsilon_o m\omega_r(\Omega - \omega_r)/e^2$. With a quadratic trapping potential the plasma has the simple shape of a spheroid, $z^2/z_o^2 + r^2/r_o^2 = 1$, where the aspect ratio $\alpha \equiv z_o/r_o$ depends on ω_r [24,26]. This is because the radial binding force of the trap is determined by the Lorentz force due to the plasma's rotation through the magnetic field. Thus low ω_r results in a lenticular plasma (an oblate spheroid) with large radius. As ω_r increases, r_o shrinks and z_o grows, resulting in an increasing α. However, large ω_r ($\omega_r > \Omega/2$) produces a large centrifugal acceleration which opposes the Lorentz force, and lenticular plasmas are once again obtained for $\omega_r \sim \Omega - \omega_m$. In our work, torques from a laser or a rotating electric field control ω_r and therefore the plasma density and shape. The plasma shape is observed by imaging the ion fluorescence scattered perpendicularly to $\mathbf{B}_o$ with an f/5 objective. (See Fig. 1.) All possible values of ω_r from ω_m to $\Omega - \omega_m$ have been accessed using both methods of applying a torque [22,27,28]. Azimuthally segmented compensation electrodes located between the main trap electrodes are used to apply the rotating electric-field perturbation. Both rotating quadrupole (see inset in Fig. 1) and dipole fields (not shown in Fig. 1) have been used to control ω_r. Below we explain how the rotating quadrupole field provides precise control of ω_r.

BRAGG SCATTERING

BCC Crystals

An infinite OCP with $\Gamma \gtrsim 170$ is predicted to form a bcc lattice. However, the bulk energies per ion of the face-centered-cubic (fcc) and hexagonal-close-packed

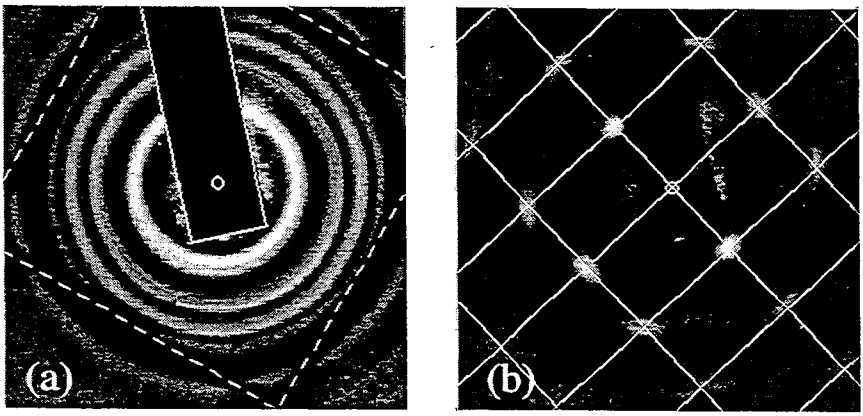

FIGURE 2. Bragg diffraction patterns from a plasma phase locked to a rotating quadrupole field ($\omega_r = 2\pi \times 140$ kHz, $n_o \approx 4.26 \times 10^8$ cm^{-3}, $\alpha \approx 1.1$). (a) 1 s time-averaged pattern. The long rectangular shadow (highlighted by solid lines) is from the deflector for the incident beam; four line shadows (highlighted by dashed lines) that form a square are due to a wire mesh at the exit window of the vacuum chamber. The small open circle near the center of the figure marks the position of the undeflected laser beam. (b) Time-resolved pattern obtained nearly simultaneously with (a) by strobing the camera with the rotating field (integration time ≈ 5 s). A spot is predicted at each intersection of the rectangular grid lines for a bcc crystal with a [110] axis aligned with the laser beam. The grid spacings were determined from the n_o calculated from ω_r and are not fitted. From Ref. [22].

(hcp) lattices differ very little from bcc ($< 10^{-4}$) [29]. Because some of the fcc and hcp planes have lower surface energies than any of the bcc planes, a boundary can have a strong effect on the preferred lattice structure. One calculation [29] estimates that the plasma may need to be $\gtrsim 100 a_{WS}$ across its smallest dimension to exhibit bulk behavior. For a spherical plasma this corresponds to $\sim 10^5$ ions.

We used Bragg scattering to measure the spatial correlations of approximately spherical plasmas with $N > 2 \times 10^5$ trapped Be^+ ions [19,20]. The cooling-laser beam directed along the trap axis was used for Bragg scattering as indicated in Fig. 1. First the plasma shape was set to be approximately spherical. (In early experiments this was done with the perpendicular laser beam; more recent experiments used the rotating wall.) The parallel laser beam was then tuned approximately half a linewidth below resonance, and a Bragg-scattering pattern recorded (~1–30 s integration). The plasma was then heated and recooled, and another Bragg-scattering pattern was recorded. Because the 313 nm wavelength of the cooling laser is small compared to the inter-ion separation (~10–20 μm), Bragg scattering occurs in the forward (few degree) scattering direction. In order for a diffracted beam to form, the incident and scattered wave vectors $\mathbf{k}_i$ and $\mathbf{k}_s$ must differ by a reciprocal lattice vector (Laue condition) [30]. In a typical x-ray crystal diffrac-

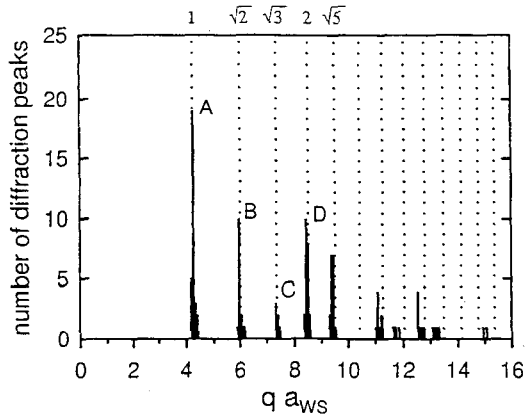

FIGURE 3. Histogram showing the numbers (not intensities) of peaks observed as a function of $q \cdot a_{WS}$ (defined in the text) for 30 time-averaged Bragg scattering patterns obtained on two different spherical plasmas with $N > 2 \times 10^5$. The dotted lines show the expected peak positions for a bcc crystal, normalized to the center of gravity of the peak at A (corresponding to Bragg reflections off {110} planes). From Ref. [20].

tion case, satisfying the Laue condition for many reciprocal lattice vectors requires that the incident radiation have a continuous range of wavelengths. Here the Laue condition is relaxed because of the small size of the crystal, so a crystalline Bragg diffraction pattern is frequently obtained even with monochromatic radiation.

Figure 2(a) shows a time-averaged diffraction pattern obtained on a spherical plasma with $N \sim 7.5 \times 10^5$. The multiple concentric rings are due to Bragg scattering off different planes of a crystal. A concentric ring rather than a dot pattern is observed because the crystal was rotating about the laser beam. In general, many different patterns were observed, corresponding to Bragg scattering off crystals with different orientations. Figure 3 summarizes the analysis of approximately 30 time-averaged patterns obtained on two different spherical plasmas with $N > 2 \times 10^5$. It shows the number of Bragg peaks as a function of the momentum transfer $q = \mid \mathbf{k}_s - \mathbf{k}_i \mid = 2k \sin(\theta_{scatt}/2)$ ($\simeq k\theta_{scatt}$ for $\theta_{scatt} \ll 1$), where $k = 2\pi/\lambda$ is the laser wave number and θ_{scatt} is the scattering angle. The density dependence of the Bragg peak positions is removed by multiplying q by a_{WS}, which was determined from ω_r. The positions of the peaks agree with those calculated for a bcc lattice, within the 2.5% uncertainty of the angular calibration. They disagree by about 10% with the values calculated for an fcc lattice. The ratios of the peak positions of the first five peaks agree within about 1% with the calculated ratios for a bcc lattice. This provides strong evidence for the formation of bcc crystals in spherical plasmas with $N > 2 \times 10^5$ ions. This result is significant because it is the first evidence for bulk behavior in a strongly coupled OCP in the laboratory.

Rotating Wall

By strobing the camera recording the Bragg-scattering pattern synchronously with the plasma rotation, we should be able to recover a dot pattern from the time-averaged concentric ring pattern in Fig. 2(a). Initially we used the time dependence of the Bragg-scattered light to sense the phase of the plasma rotation [20,31]. More recently we used a rotating electric-field perturbation to phase-lock the ion plasma rotation [21,22].

Consider the rotating quadrupolar perturbation shown in the inset of Fig. 1. This z-independent perturbation produces a small distortion in the shape of the spheroidal plasma. In particular, the plasma acquires a small elliptical cross section normal to the z-axis. (In our work the distortion created by the rotating quadrupole field was typically less than 1% of the plasma diameter.) The elliptical boundary rotates at the applied rotating wall frequency ω_w. An ion near the plasma boundary experiences a torque due to this rotating boundary. If the ion is rotating slower than ω_w, the torque will speed it up. If it is rotating faster than ω_w, the torque will slow it down. Through viscous effects, this torque is transmitted to the plasma interior. Therefore, if other external torques are small, the rotating wall perturbation will make ω_r equal ω_w. Crystallized plasmas behave more like a solid than a liquid or gas. Because the viscosity is high, the whole plasma tends to rotate rigidly with its boundary. In particular, the orientation of the ion crystals can phase-lock to the rotating quadrupolar perturbation if the difference between ω_r and ω_w is small.

To check for phase-locked control of ω_r, we strobed the camera recording the Bragg-scattering pattern in Fig. 2(a) with the synthesizer used to generate the rotating wall signal. Specifically, once each $2\pi/\omega_w$ period, the rotating wall signal gated the camera on for a period $\lesssim 0.02(2\pi/\omega_w)$. The resulting Laue dot pattern in Fig. 2(b) shows that the plasma rotation was phase-locked to the rotating electric-field perturbation. The dot pattern provides detailed information on the number and orientation of the crystals which contributed to the Bragg-scattering signal. For example, the pattern in Fig. 2(b) was due to a single bcc crystal with a [110] axis aligned along the laser beam. For phase-locked operation of the rotating wall, other external torques must be small. For example, a misalignment of the trap magnetic field with the trap-electrode symmetry axis of $> 0.01°$ prevented phase-locked control of the plasma rotation. In our work, alignment to $\lesssim 0.003°$ was obtained by minimizing the excitation of zero-frequency plasma modes [27,28].

In addition to the rotating quadrupole perturbation, phase-locked control was also achieved with a uniform rotating electric field (a "dipole" field). In fact under many circumstances a uniform oscillating field worked equally well. In these cases the co-rotating component of the oscillating field controlled the plasma rotation, while the perturbing effects due to the counter-rotating component were minimal. For further discussion, see Ref. [22].

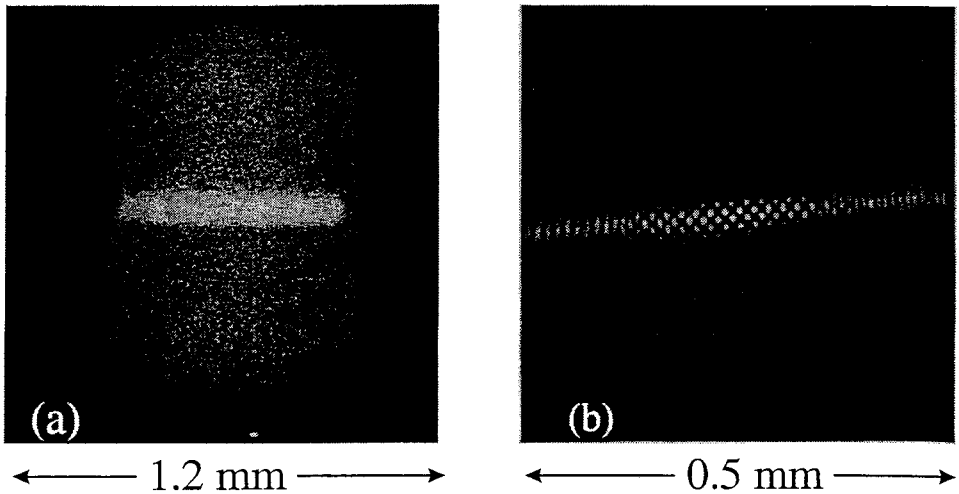

FIGURE 4. Real-space images of an $N \sim 1.8 \times 10^5$ ion plasma phase-locked with an oscillating dipole field at $\omega_r = 2\pi \times 120$ kHz. (a) Time-averaged side-view image showing the overall plasma shape. The bright line of fluorescence through the plasma center is due to a laser beam directed perpendicularly to $\mathbf{B_o}$. The plasma shape is approximately spherical. The presence of heavier-mass ions, which centrifugally separate from the $^9Be^+$ ions, produces the straight vertical boundaries in the image. (b) Strobed top-view image, obtained simultaneously with (a), showing the presence of a bcc crystal in the plasma center. The distance scales in (a) and (b) are different, as noted.

REAL-SPACE IMAGES

Bragg scattering measures the Fourier transform of the spatial correlations of the trapped ions. It provides a picture of these correlations in reciprocal-lattice space. With phase-locked control of ω_r, real-space imaging of individual ions in a Penning trap becomes possible. To obtain real-space images with high resolution, we replaced the Bragg scattering optics (see Fig. 1) with imaging optics, starting with an f/2 objective, which formed a real, top-view image of the ion plasma. The combined resolution limit of the optics and camera was less than 5 μm near the optimal object plane of the f/2 objective. This is less than the $\sim$10 μm resolution limit required to resolve individual ions. However, the depth of field of an f/2 objective for 10 μm resolution is $\sim$80 μm. For lenticular plasmas with $2z_o \lesssim 80$ μm, all of the ions within the plasma were resolvable. For plasmas with $2z_o > 80$ μm, the cooling-laser beam directed perpendicularly to $\mathbf{B_o}$ was used to illuminate a section of the plasma within the depth of field.

Figure 4 shows side-view and top-view images of an approximately spherical plasma with $N \sim 1.8 \times 10^5$. The fluorescence from the perpendicular laser beam used to highlight a small region of the plasma is clearly visible. In the top-view

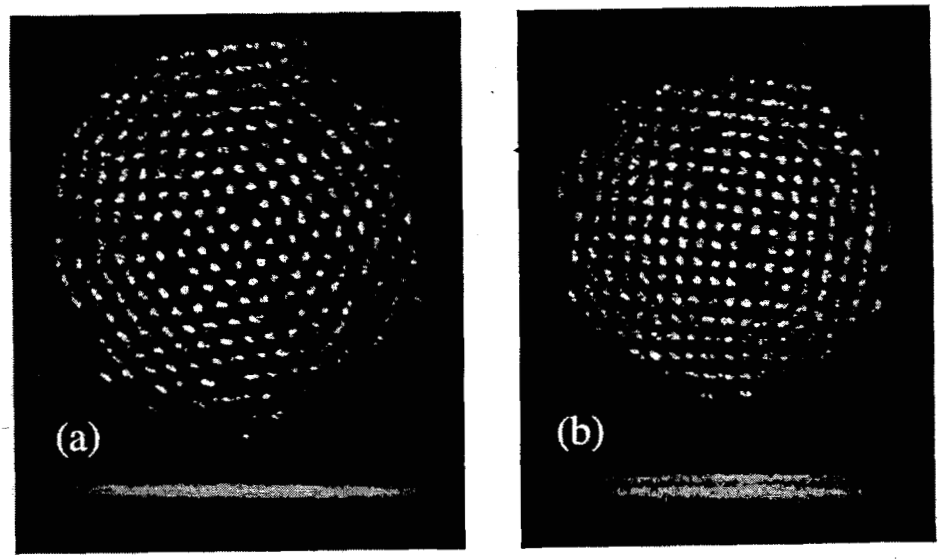

FIGURE 5. Strobed top-view images of a small ($N \sim 300$ Be^+) ion plasma phase-locked with a rotating dipole field at (a) $\omega_r = 2\pi \times 65.7$ kHz and (b) 66.5 kHz. Below are unstrobed side-views showing the axial lattice planes. Heavier-mass ions are located outside the $^9Be^+$ ions.

image a square grid of dots is observed near the plasma center. The measured spacing between nearest neighbor dots is 12.8 ± 0.3 μm, in good agreement with the 12.5 μm spacing expected for viewing along a [100] axis of a bcc crystal with density determined by the ω_r set by the rotating field. Real-space imaging provides direct information on the location and size of the crystals. In Fig. 4 the crystal was located in the radial center of the plasma and was at least 230 μm across, or at least 1/4 of the plasma diameter.

For lenticular plasmas with $2z_o \lesssim 80$ μm, all of the ions within the plasma are resolved without the use of the perpendicular laser beam. Lenticular plasmas are obtained with ω_r slightly greater than ω_m. For small plasmas ($N \lesssim 2000$ ions) we were able to use the rotating-dipole electric field to lower ω_r and obtain a single plane while maintaining long-range order in the top-view images. Figure 5(a) shows top- and side-view images of such a plasma. Near the plasma center a 2-D hexagonal lattice is observed, the preferred lattice for a 2-D system. Here each dot is the image of an individual ion.

Starting with a single plane like that shown in Fig. 5(a), we studied the structural phase transitions that occur as ω_r is increased [23]. With increasing ω_r, the radial confining force of the Penning trap increases, which decreases r_o. At a particular point, there is a structural phase transition near the plasma center from a single, hexagonal lattice plane to two lattice planes where the ions form a square grid in each plane, as shown in Fig. 5(b). Further increases in ω_r increase the number of

ions per unit area of each plane as well as the spacing between the planes. During this process the square lattice planes smoothly change into rhombic lattice planes and eventually there is a sudden transition to hexagonal lattice planes. Further increases in ω_r eventually produce a structural transition to three square lattice planes, and the basic pattern repeats.

The structure of the crystallized ions depends sensitively on the projected areal density σ of the plasma. The side- and top-view images were analyzed to characterize the phase structure. Within a layer, the structural order is characterized by the primitive vectors $\mathbf{a_1}$ and $\mathbf{a_2}$ (which are observed to be equal in magnitude) and the angle θ ($\leq 90°$) between them. The interlayer order is characterized by the axial positions z_n of the n lattice planes (measured by the side-view camera) and the interlayer displacement vector $\mathbf{c_n}$ between layers 1 and n. Hence, the equilibrium positions in the (x, y) plane of ions in axial planes 1 and n are given by $\mathbf{R_1} = i\mathbf{a_1} + j\mathbf{a_2}$ and $\mathbf{R_n} = i\mathbf{a_1} + j\mathbf{a_2} + \mathbf{c_n}$, where i, j are integers. Three different types of intralayer ordering are observed: hexagonal ($\theta = 60°$), square ($\theta = 90°$) and rhombic ($90° > \theta \geq 65°$). The observations were compared to the results from Dubin [23], who performed an analytic calculation of the energies of lattice planes which are infinite and homogeneous in the (x, y) direction but are confined in the axial direction by a harmonic external electrostatic confinement potential $\phi_e = 1/2(m/e)\omega_z^2 z^2$. Since this potential is identical to the confinement potential of a Penning trap as seen in the rotating frame in the $\alpha \to 0$ planar limit, the minimum-energy phase structures predicted by the theory should match the structures observed in the central regions of the oblate plasmas of the experiments.

Figure 6 displays the agreement between theory and experiment for the interlayer quantities, with measurements taken on different plasmas with $N < 10^4$. Lengths have been normalized by $a_{ws2D} = (3e^2/4\pi\epsilon_0 m\omega_z^2)^{1/3} = 10.7$ μm, which is the Wigner-Seitz radius in the planar limit. As the central areal density is increased the lattice planes move further apart axially in order to match their average density to the neutralizing background. Eventually it becomes energetically favorable to form an additional lattice plane. The symbols indicate whether the lattices had an interlattice displacement vector $\mathbf{c_2}$ characteristic of the hexagonal phases (triangles) or the square and rhombic phases (squares).

Figure 7 displays the agreement between experiment and theory for the dependence of the angle θ (between the primitive vectors) on central areal charge density σ. The trend is that when a new lattice plane is formed, θ changes discontinuously from $\approx 60°$ to a higher value. As the central areal density of the crystal is further increased, θ smoothly decreases to $\approx 65°$ until there is a second discontinuous transition to a hexagonal structure. This latter transition has been predicted [32] to become continuous in liquid ($\Gamma < 80$) bilayer systems. The lines indicate the minimum energy structures predicted by the 2D theory.

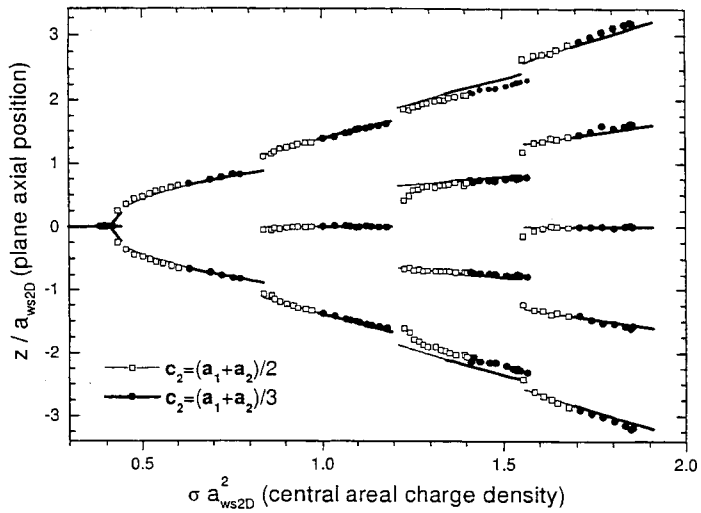

FIGURE 6. Interlayer structure (plane axial positions and displacement vectors) as a function of normalized areal charge density. The lines are the predictions of theory, and the symbols are experimental measurements.

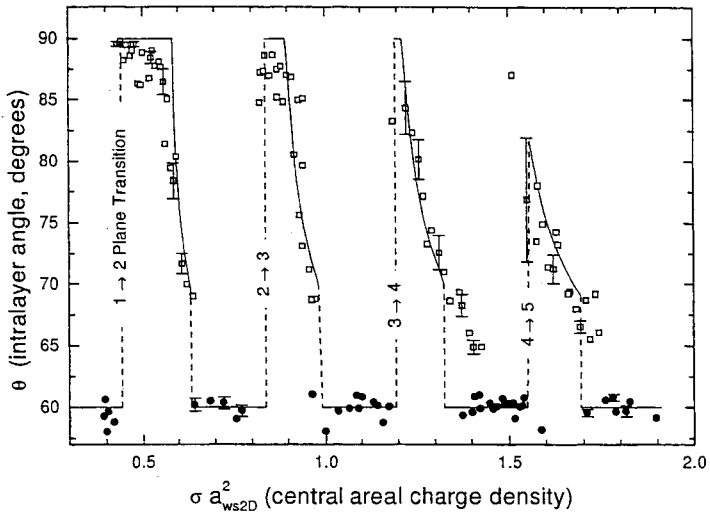

FIGURE 7. Intralayer angle θ structure as a function of normalized areal charge density. The lines are the predictions of theory, and the symbols are experimental measurements. Representative error bars are included with some of the measurements.

DISCUSSION

With Bragg scattering and spatial imaging, we have measured the correlations in both spherical and highly oblate strongly coupled $^9Be^+$ ion plasmas. The planar geometry permits a detailed comparison with theoretical calculations. We have measured the preferred lattice structures for up to five lattice planes in lenticular plasmas and obtain good agreement with theory. Ions in a trap have been proposed as a register for a quantum computer [33]. Work in this area has focussed on a string of a few ions in a linear Paul trap [34]. A single lattice plane of ions as in Fig. 5 could provide a 2-D geometry of trapped ions for studies of quantum computing or entangled quantum states.

In spherical plasmas with more than 2×10^5 ions, we have observed the formation of bcc crystals, the predicted state for the infinite strongly coupled OCP. The crystals occupied the inner quarter of the plasma diameter. Outside the crystal there was a complicated transition to shell structure. In this system we have not observed the thermodynamic liquid-solid phase transition predicted for the bulk OCP. The phase transition may take place in the present system, but we have experimentally missed detecting it. Or, possibly larger crystals (for example, where the number of ions in the crystal is large compared to the number of ions in the shells) may be required in order for a sharp phase transition to be exhibited.

We have observed structures for which we do not have a good theoretical understanding. Figure 8(a) shows an approximate fivefold Bragg-scattering pattern that was observed a number of times under different experimental circumstances. A fivefold Bragg-scattering pattern is characteristic of a quasi-crystal. However, more sets of dots would be present in a true quasi-crystalline Bragg-scattering pattern. We now think that the fivefold Bragg-scattering pattern of Fig. 8(a) is due to a structure like that shown in Fig. 8(b). Figure 8(b) is a top-view image of a lenticular plasma which consisted of four horizontal planes. Even though it is difficult to distinguish individual ions in this figure, it is possible to see that there are five distinct regions where the ions resided in vertical planes. The planes from these different regions form a five-sided structure that would produce a Bragg scattering pattern like Fig. 8(a). Once formed, this fivefold structure was stable.

In addition to enhancing studies of Coulomb crystals, the phase-locked control of ω_r has improved the prospects of a microwave frequency standard based on a hyperfine-Zeeman transition of ions stored in a Penning trap. This is because the time-dilation shift due to the plasma rotation is one of the largest known systematic shifts in such a standard. Reference [35] discusses the potential frequency stability and accuracy of a microwave frequency standard based on 10^6 trapped ions. For ions such as $^{67}Zn^+$ and $^{201}Hg^+$, fractional frequency stabilities $\lesssim 10^{-14}/\tau^{1/2}$ with time-dilation shifts due to the plasma rotation of $\sim$few$\times 10^{-15}$ are possible. Here τ is the measurement time in seconds. With phase-locked operation of the rotating wall, we think it should be possible to stabilize and evaluate the rotational time-dilation shift within 1%. Therefore the inaccuracy due to this shift would contribute a few parts in 10^{-17}.

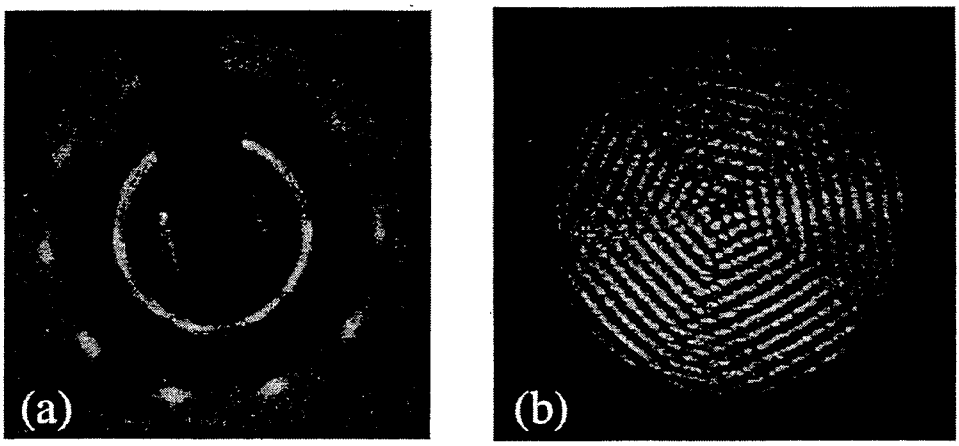

FIGURE 8. Fivefold Bragg scattering and real-space patterns obtained by strobing the intensified CCD camera synchronously with the rotating electric field perturbation. (a) Bragg scattering pattern obtained on an $N \sim 1.2 \times 10^5$ ion plasma phase-locked with a rotating dipole field at $\omega_r = 2\pi \times 166.84$ kHz. Here $V_o = 500$ V and $\alpha = 2.6$. (b) Real-space image of a lenticular plasma consisting of 4 horizontal planes in the plasma center. The rotating dipole field was used to set $\omega_r = 2\pi \times 74.35$ kHz.

ACKNOWLEDGEMENTS

We gratefully acknowledge the support of the Office of Naval Research. We thank S. L. Gilbert and R. J. Rafac for their comments on the manuscript.

REFERENCES

1. Bollinger, J. J., *et al.*, in *Trapped Charged Particles and Fundamental Physics*, Dubin, D. H. E., and Schneider, D., ed. AIP, New York: 1999, pp. 295–304.
2. Mitchell, T. B., *et al.*, *Phys. Plasmas* **6**, 1751 (1999).
3. Ichimaru, S., Iyetomi, H., and Tanaka, S., *Phys. Rep.* **149**, 91–205 (1987).
4. Malmberg, J. H., and O'Neil, T. M., *Phys. Rev. Lett.* **39**, 1333–1336 (1977).
5. Horn, H. M. V., *Science* **252**, 384–389 (1991).
6. Grimes, C. C., and Adams, G., *Phys. Rev. Lett.* **42**, 795–798 (1979).
7. E. L. Pollock and J. P. Hansen, *Phys. Rev. A* **8**, 3110–3122 (1973); W. L. Slattery, G. D. Doolen, and H. E. DeWitt, *ibid.* **21**, 2087–2095 (1980); W. L. Slattery, G. D. Doolen, and H. E. DeWitt, *ibid.* **26**, 2255–2258 (1982); S. Ogata and S. Ichimaru, *ibid.* **36** 5451–5454 (1987); G. S. Stringfellow and H. E. DeWitt, *ibid.* **41**, 1105–1111 (1990); D. H. E. Dubin, *ibid.* **42**, 4972–4982 (1990).
8. Schiffer, J. P., *Science* **279**, 675 (1998).
9. Diedrich, F., *et al.*, *Phys. Rev. Lett.* **59**, 2931–2934 (1987).

10. Wineland, D. J., *et al.*, *Phys. Rev. Lett.* **59**, 2935–2938 (1987).
11. Strongly coupled clusters of highly charged, micrometer-sized aluminum particles were previously observed in Paul traps. See R. F. Wuerker, H. Shelton, and R. V. Langmuir, *J. Appl. Phys.* **30**, 342–349 (1959).
12. Gilbert, S. L., Bollinger, J. J., and Wineland, D. J., *Phys. Rev. Lett.* 2022-2025 (1988).
13. Birkl, G., Kassner, S., and Walther, H., *Nature* **357**, 310–313 (1992).
14. Drewsen, M., *et al.*, *Phys. Rev. Lett.* **81**, 2878 (1998).
15. Walther, H., *Adv. At. Opt. Phys.* **31**, 137–182 (1993).
16. Melzer, A., Homann, A., and Piel, A., *Phys. Rev. E* **53**, 2757 (1996).
17. Murray, C. A., and Grier, D. G., *American Scientist* **83**, 238–245 (1995).
18. Vos, W. L., Mehens, M., van Kats, C. M., and Bösecke, P., *Langmuir* **13**, 6004–6008 (1997).
19. Tan, J. N., Bollinger, J. J., Jelenković, B., and Wineland, D. J., *Phys. Rev. Lett.* **75**, 4198-4201 (1995).
20. Itano, W. M., *et al.*, *Science* **279**, 686–689 (1998).
21. Huang, X.-P., Bollinger, J. J., Mitchell, T. B., and Itano, W. M., *Phys. Rev. Lett.* **80**, 73–76 (1998).
22. Huang, X.-P., Bollinger, J. J., Mitchell, T. B., and Itano, W. M., *Phys. Plasmas* **5**, 1656–1663 (1998).
23. Mitchell, T. B., *et al.*, *Science* **282**, 1290 (1998).
24. Brewer, L. R., *et al.*, *Phys. Rev. A* **38**, 859–873 (1988).
25. Davidson, R. C., *Physics of Nonneutral Plasmas* Addison-Wesley Publishing: 1990, pp. 39–75.
26. O'Neil, T. M., and Dubin, D. H. E., *Phys. Plasmas* **5**, 2163–2193 (1998).
27. Heinzen, D. J., *et al.*, *Phys. Rev. Lett.* **66**, 2080–2083 (1991).
28. Bollinger, J. J., *et al.*, *Phys. Rev. A* **48**, 525–545 (1993).
29. Dubin, D. H. E., *Phys. Rev. A* **40**, 1140–1143 (1989).
30. Ashcroft, N. W., and Mermin, N. D., *Solid State Physics* Saunders College: 1976, pp. 95–110.
31. Tan, J. N., *et al.*, in *Proceedings of the International Conference on Physics of Strongly Coupled Plasmas*, Kraeft, W. D., and Schlanges, M., ed. World Scientific: 1996, pp. 387–396.
32. Valtchinov, V. I., Kalman, G., and Blagoev, K. B., *Phys. Rev. E* **56**, 4351–4355 (1997).
33. Cirac, J. I., and Zoller, P., *Phys. Rev. Lett.* **74**, 4091–4094 (1995).
34. Wineland, D. J., *et al.*, *J. Res. Natl. Inst. Stand. Technol.* **103**, 259–328 (1998).
35. Tan, J. N., Bollinger, J. J., and Wineland, D. J., *IEEE Trans. Instrum. Meas.* **44**, 144–147 (1995).